Article

C$_{60}$ Fullerene-Reinforced Silicon Oxycarbide Composite Fiber Mats: Performance as Li-Ion Battery Electrodes

Arijit Roy, Shakir Bin Mujib, and Gurpreet Singh*

Cite This: *ACS Omega* 2024, 9, 35757−35768

Read Online

ACCESS | Metrics & More | Article Recommendations | Supporting Information

ABSTRACT: Precursor-derived silicon oxycarbide (SiOC) has emerged as a potential high-capacity anode material for rechargeable Li-ion batteries. The polymer processing and pyrolysis route, a hallmark of polymer-derived ceramics, allows chemical interfacing with a variety of nanoprecursors and nanofiller phases to produce composites with low-dimensional structures such as fibers and coatings not readily attained in traditional sintered ceramics. Here, buckminsterfullerene or C$_{60}$ was introduced as a filler phase in a hybrid precursor of 1,3,5,7-tetramethyl-1,3,5,7-tetravinyl-cyclotetrasiloxane (TTCS) along with polyvinylpyrrolidone or PVP as a spinning agent to fabricate electrospun fiber mats, which upon a high-heat treatment transformed to a C$_{60}$-reinforced SiOC ceramic composite. Tested as the self-supporting working electrode in a Li-ion half-cell, C$_{60}$-reinforced fiber mats show a much-improved reversible capacity (825 mA h g^{-1}), nearly 100% Coulombic efficiency, and superior rate capability with low-capacity decay at high currents (only 25.5% decay at 800 mA g^{-1}) compared to neat C$_{60}$ and neat carbonized fiber electrodes.
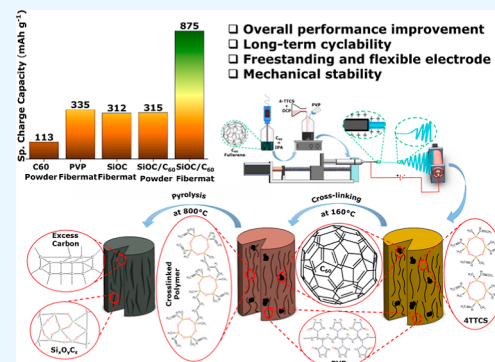
1. INTRODUCTION

The X-ray amorphous covalent ceramics derived from the polymer pyrolysis route, also known as polymer-derived ceramics (PDCs), have been studied extensively as potential anode materials in LIBs. Amorphous SiOC is one such ceramic that has shown high Li-insertion capacity due to the presence of silicon suboxides, silicon mixed bonding with carbon and oxygen, and the presence of graphitic or string-like carbon phases.[1−3] The amorphous structure of the PDC electrode provides stability toward repeated cycling of Li ions by accommodating volume changes upon lithium insertion and forming a stable solid electrolyte interphase (SEI) layer. However, SiOC electrodes in LIBs suffer from high first-cycle loss, poor charge transfer characteristics, and high-voltage hysteresis.[4−6] To overcome such shortcomings, polymer precursors have been modified with dopant atoms and nanoscale conducting fillers of varying sizes, shapes, and configurations to produce composite ceramic architectures.[7−9] For example, authors[10] investigated SiOC-graphene composite paper electrodes to achieve a charge capacity of 588 mA h g^{-1} over 1000 cycles and showed no evidence of mechanical failure in LIBs. Dey et al.[11] studied SiOC-functionalized MoSe$_2$ to show better lithium cycling stability than neat electrodes (both MoSe$_2$ and SiOC) over 100 cycles. In addition, several studies have reported the hybridization of PDCs (SiOC and SiCN) with nanomaterials such as carbon nanotubes (CNTs),[12] boron,[13] tin (Sn),[14] aluminum,[15] reduced-graphene oxide,[16] graphene nanoplatelets,[17] and Li metal[18] to achieve improved electrical conductivity, cycling efficiency, and long-term stability. However, other exotic and more diverse molecular

forms of carbon, such as the C$_{60}$ buckminsterfullerene,[19,20] carbon graphene,[21] carbon nanohorns,[22] and amorphous carbon particles,[23] which have the potential to influence the evolution of microstructure (including nanovoid and silicon mixed bonding) and chemical composition of the ceramic phase during pyrolysis are rarely studied. Such carbons may act as a potential filler phase for even more favorable electronic and thermodynamic properties of PDC electrodes.

Existing literature on the use of neat C$_{60}$ electrodes for LIBs suggests a high capacity for Li ions. However, poor reversible capacity and an unstable secondary electrolyte layer (SEI) tend to limit the efficiency of cycling of Li ions in subsequent cycles.[24−26] Specifically, a study by Seger et al., which tested a solid C$_{60}$ film as an anode in LIBs, concluded that the dissolution of C$_{60}$ supermolecules in the electrolyte resulted in poor stability of the highly reduced material and limited its use.[27] Later, Tan et al.[28] utilized KOH activation of C$_{60}$ in an ammonia atmosphere to achieve nitrogen-doped C$_{60}$ and achieved a reversible capacity of up to 1900 mA h g^{-1} at 100 mA g^{-1} in LIBs. Park et al.[29] investigated a highly conductive cocrystal of C$_{60}$ and contorted hexabenzocoronene (cHBC) as an anode for LIBs. The cocrystal structure of C$_{60}$/cHBC was
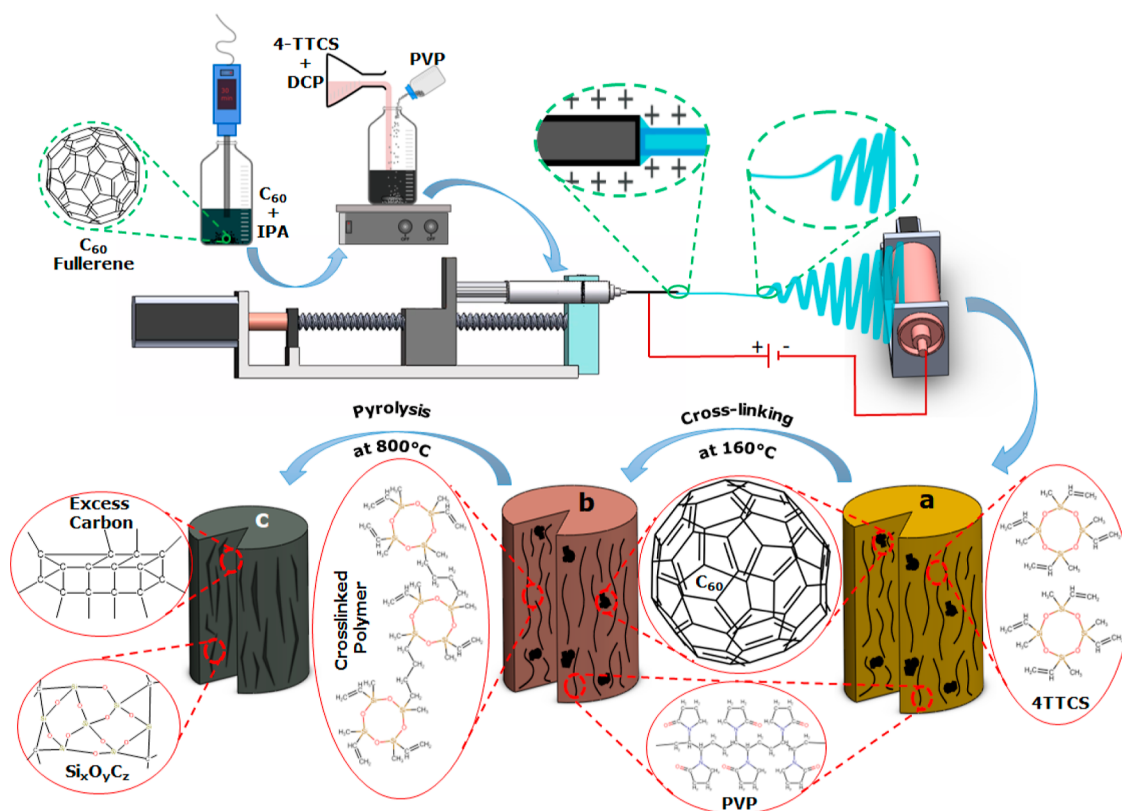
Figure 1. Schematic for the fabrication of the SiOC/C$_{60}$ fiber mat shows the step-by-step process of electrode preparation: (a) electrospun fiber, (b) cross-linked fiber, and (c) pyrolyzed fiber.

found to provide reliable vacant sites for Li$^+$ storage, resulting in a reversible capacity of 330 mA h g^{-1} at 100 mA g^{-1} for up to 600 cycles. Overall, chemically modified C$_{60}$-based electrodes have been found to be more effective than neat C$_{60}$ for realizing high performance in LIBs.[11,12,30]

Motivated by these previous studies, herein, we report on the introduction of buckminsterfullerene or C$_{60}$ nanoparticles in cyclic siloxane to produce nonwoven electrospun SiOC/C$_{60}$ fiber mats upon pyrolysis and report on their performance as the electrodes for LIBs. The as-synthesized SiOC/C$_{60}$ fiber mat was characterized by using several microscopic and spectroscopic techniques to investigate the microstructures and chemical compositions of the materials. As an anode, the SiOC/C$_{60}$ electrode showed a first-cycle capacity of 1211 mA h g^{-1} with a high Coulombic efficiency of 65%. The composite electrode also showed a higher capacity retention than the neat SiOC and C$_{60}$ electrodes over 175 cycles. This is the first study to report a flexible SiOC/C$_{60}$ composite (free of binder and conductive agents) as an anode material for LIBs.

2. MATERIALS, METHODS, AND CHARACTERIZATION

2.1. Materials. The fullerene-C$_{60}$ powder with a molecular weight of 720.64, spinning agent polyvinylpyrrolidone (PVP) with an average molecular mass of 1,300,000 g mol^{-1}, and cross-linking agent dicumyl peroxide (DCP) were purchased from Sigma-Aldrich (St. Louis, MO, USA). The preceramic silicon oligomer 1,3,5,7-tetramethyl, 1,3,5,7-tetravinyl cyclo-tetrasiloxane, denoted as 4-TTCS, was purchased from Gelest (Morrisville, PA, USA). The solvent, isopropyl alcohol (IPA), was purchased from Fisher Chemical (Lenexa, KS, USA). The conducting agent carbon black (C/B) and binder poly-(vinylidene fluoride) (PVDF) were purchased from Alfa

Aesar (Massachusetts, USA). N-Methyl-2-pyrrolidinone (NMP) was bought from Sigma-Aldrich (Missouri, USA). The ultrahigh-purity argon gas used in the glovebox was purchased from Matheson (Manhattan, KS, USA).

2.2. Methods. *2.2.1. C$_{60}$ on Cu Foil.* The C$_{60}$ electrode on copper foil was prepared using 80 wt % C$_{60}$, 10 wt % PVDF as a binder, and 10 wt % C/B as a conducting agent. A few drops of NMP were incorporated to obtain a homogeneous slurry. The slurry was then coated onto a Cu foil with a thickness of 9 μm and dried overnight at 80 °C. A circular electrode with a diameter of 14.29 mm was punched out of the coated Cu foil.

2.2.2. Electrospinning. The fabrication process of PDC fibers started with spinning the fiber, which was generated from a preceramic polymer precursor in a sol–gel state. The raw material for fiber production necessitates certain properties; i.e., as a liquid, it should exhibit flowability or viscoelasticity and possess solubility in specific solvents. Such qualities facilitate the preparation of a homogeneous solution for spinning and optimal fiber production. The fiber mat fabrication process is discussed below, and other parametric details of electrospinning are mentioned in the Supporting Information (Section 1).

2.2.3. PVP Fiber Mat Preparation. The solution for the PVP fiber mat was prepared with 800 mg of PVP powder and IPA with a PVP: IPA concentration of approximately 85:1 mg mL^{-1}. The solution was stirred for 2 h with a magnetic stirrer to generate a homogeneous mixture, which was then collected into a 10 mL syringe with a metallic needle for electrospinning. The produced fiber mat was referred to as the PVP fiber mat in the following sections.

2.2.4. SiOC/C$_{60}$ Fiber Mat Preparation. In the initial step of preparing the SiOC/C$_{60}$ fiber mat, a solution was developed by
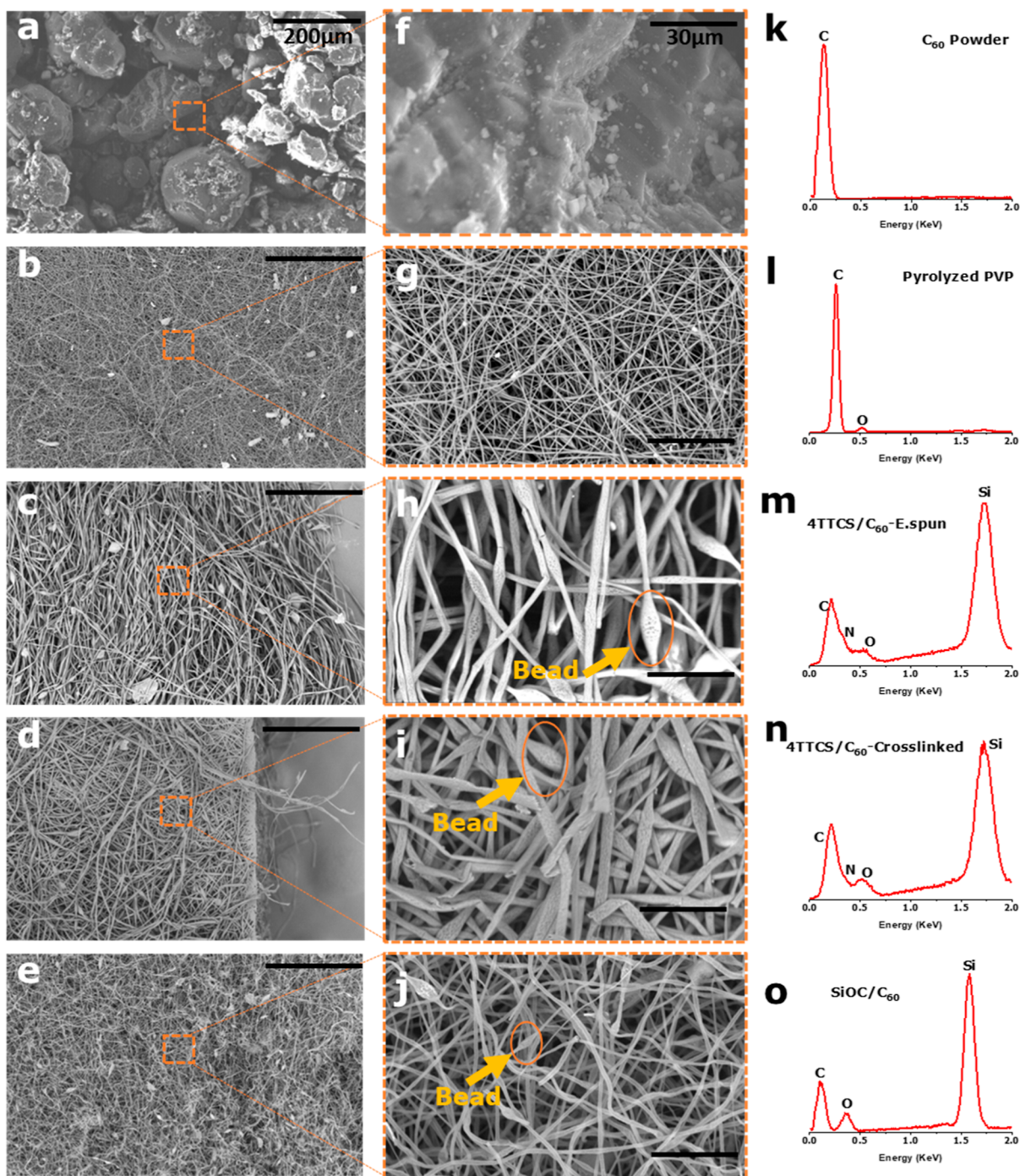
Figure 2. SEM images of (a) C_{60} powder, (b) pyrolyzed PVP fiber mat, (c) 4TTCS/C_{60} electrospun fiber mat, (d) 4TTCS/C_{60} cross-linked fiber mat, (e) SiOC/C_{60} fiber mat, and their corresponding (f–j) high-magnification SEM images demonstrate the uniform and homogeneous morphology of dense fibers with a few beads. (k–o) The corresponding XRF spectra reveal the elemental composition, proving high purity.

mixing 90 mg of C_{60} with IPA at a C_{60}/IPA concentration of 13.1:1 mg mL^{-1} using bath sonication for 10 min followed by horn sonication for 30 min (4 min sonication and 1 min rest). Then 600 mg of PVP and another 0.51 mL of IPA were added to the solution as some of the IPA was vaporized during sonication. After magnetically stirring the solution for 1 h, 1.8 mL of the polymeric precursor 4-TTCS along with 1 wt % of DCP (i.e., 18 mg) was added, keeping C_{60}/4-TTCS at 50:1 mg mL^{-1} and again magnetically stirred for 2 h to generate a homogeneous mixture. Then, the resultant solution was further loaded into a similar syringe for SiOC/C_{60} fiber mat

electrospinning. The schematic in Figure 1 demonstrates the major parts and steps of the electrospinning process.

The fiber mat fabrication process from the solution-loaded syringe was similar for all three kinds of fiber mats. A slow feed rate of only 5 mL h^{-1} of the solution was maintained throughout the experiments. Depending on the viscosity of the solution, a high voltage of 15–20 kV was applied between the syringe and cylindrical-shaped roller collector, with a distance of 15 cm in between. The fabricated 15 × 15 cm^2 as-spun fiber mats (Figure 1a) were kept overnight for drying in open air, denoted as e-spun 4TTCS/C_{60} fiber mats. At this stage,
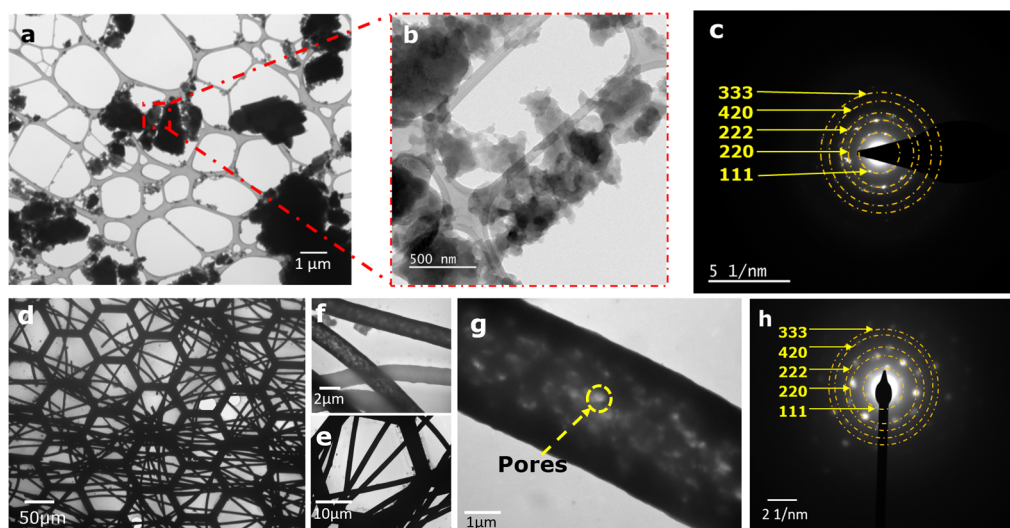
Figure 3. (a) TEM and (b) high-resolution TEM (HRTEM) show the clusters of C_{60} powder, and (c) selected area electron diffraction (SAED) pattern reveals their corresponding planes, proving a face-centered cubic (fcc) lattice. (d−f) TEM and (g) HRTEM of SiOC/C_{60} fiber mats display a long, smooth, uniform fiber morphology similar to that observed in the SEM, and (h) corresponding SAED pattern exhibits similar planes as C_{60} powder, proving the incorporation of C_{60} fullerene within the fibers.

preceramic silicon oligomers embedded in fibers exhibited initial structures that closely resemble vinyl and methyl groups, potentially serving as cross-linking sites. Then, the fiber mats were kept inside an oven at 160 °C for 24 h for cross-linking (Figure 1b), denoted as cross-linked 4TTCS/C_{60} fiber mats. The cross-linking process at 160 °C, in the presence of DCP, involved the following reaction,[31] which immobilized the 4TTCS

$$\equiv Si{-}CH_3 + CH_2{=}CH{-}Si\equiv \rightarrow \equiv Si{-}(CH_2)_3{-}Si\equiv$$
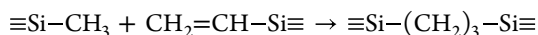
Up to this stage, the C_{60} fullerene nanoparticles remained inactive inside the fibers. The cross-linked fiber mats were then cut into smaller rectangular pieces (5.5 × 3.5 cm^2) and put into a tube furnace for pyrolysis (Figure 1c), denoted as the SiOC/C_{60} fiber mat. In an argon gas inert environment, inside the tube furnace, two-stage annealing was implemented at 400 °C for 1 h and 800 °C for 30 min, with a heating rate of 2 °C per minute. During this high-temperature carbonization of the fiber mat, the cross-linked polymers transformed into a $Si_xO_yC_z$ ceramic network. Also, after pyrolysis, free carbons originated from PVP, 4TTCS, and C_{60} nanoparticles. The thermal treatment conditions for both cross-linking and pyrolysis were the same for all fiber mats.

Circular electrodes for the coin cell assembly were punched out from the pyrolyzed fiber mats with a diameter of 7.94 mm. The mass of the pyrolyzed PVP and SiOC/C_{60} electrodes was 0.4 and 0.5 mg, respectively. Pure lithium metal foil with a diameter of 14.3 mm and a thickness of 25 μm was used as the counter electrode. 1.0 M LiPF$_6$ (lithium hexafluorophosphate) in (1:1 v/v) ethylene carbonate (EC): dimethyl carbonate (DMC) with an ionic conductivity of 10.7 mS cm^{-1} was used as the electrolyte (Sigma-Aldrich, MO, USA) for the lithium-ion half-cells. The thickness of the presoaked glass separator was 25 μm, and the diameter was 19 mm, which separated the two electrodes. All the coin cells were assembled inside the glovebox in a high-precision argon atmosphere, keeping the O$_2$ and H$_2$O content below 0.1 ppm.

2.3. Characterization Techniques. The morphology, chemical composition, and evolution of various chemical bonding states of starting precursors, C_{60} powders, and electrospun fiber mats (before and after cross-linking and pyrolyzed fiber mats) were studied by using electron microscopy and a range of spectroscopic techniques. A scanning electron microscope (SU8010, Hitachi) was used to document the features on fiber surfaces and size distribution, while a transmission electron microscope (Phillips CM100 TEM under an accelerating voltage of 100 kV) was used to obtain additional information related to the morphology and crystallinity at various locations along the fibers. Furthermore, the chemical composition of various specimens was determined by the use of an X-ray fluorescence (XRF) analyzer attached to a Hitachi SEM, SU8010, Hitachi.

Raman spectroscopy and Fourier-transform infrared (FTIR) spectroscopy were used to study the molecular structure and chemical interactions in C_{60} and various fiber mats during various stages of their processing. Raman spectroscopy was performed by using a Horiba Jobin Yvon LabRam ARAMIS system equipped with a HeNe laser source (532 nm) to evaluate carbon vibrational modes only; these modes are observed in the 800−2000 cm^{-1} wavenumber range. The presence and evolution of various chemical functional groups related to siloxane precursors in the fiber mats during cross-linking and pyrolysis were recorded by using a Thermo Scientific Nicolet iS5 (iD7 ATR) spectrometer in the 1750−500 cm^{-1} range.

Chemical composition and bonding states of silicon, carbon, and oxygen for various specimens were recorded by using X-ray photoelectron spectroscopy (XPS, Thermo Scientific) equipped with Al Kα^+ ion beam (beam energy = 1486.6 eV and spot size = 400 μm). Prior to data collection, the specimens were sputtered with Ar$^+$ at 3.0 keV for 2 min to remove surface contaminations.

3. RESULTS AND DISCUSSION

The morphological differences between the fiber mats and the C_{60} powder were investigated by using SEM. Figure 2a shows the SEM image of the C_{60} powder, and Figure 2b−e illustrates the pyrolyzed PVP fiber mat, 4TTCS/C_{60} electrospun fiber
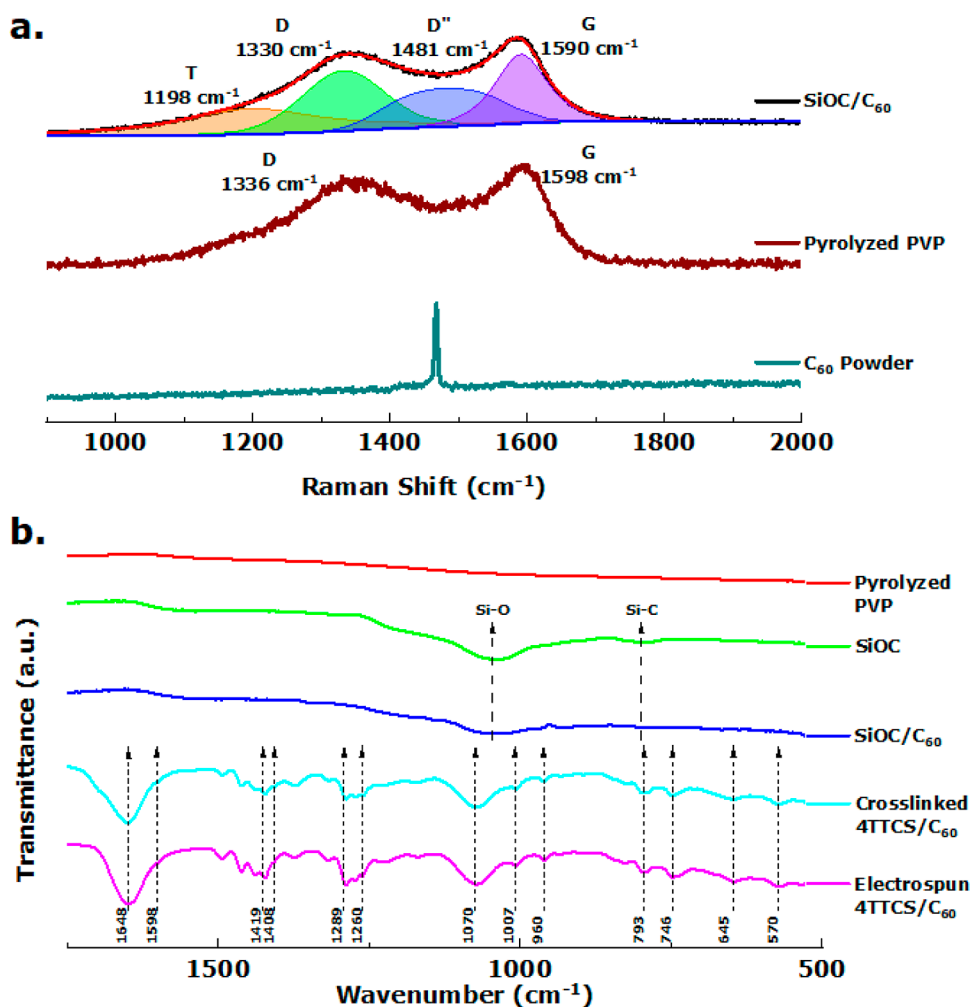
Figure 4. Raman spectra of (a) neat C_{60} powder, pyrolyzed PVP fiber mat, and curve-fitted SiOC/C_{60} fiber mat, which demonstrates the characteristics of D, D″, G, and T band vibrational peaks with relative peak sharpness and positions. (b) FTIR spectra of the pyrolyzed PVP fiber mat, SiOC fiber mat, and the as-spun, cross-linked, and pyrolyzed SiOC/C_{60} fiber mats with labeling of the bond of Si−O and Si−C.

mat, cross-linked fiber mat, and pyrolyzed SiOC/C_{60} fiber mat, respectively. Also, Figure 2f−j presents their corresponding high-magnification SEM images. The large-size C_{60} clusters are not observable in the SiOC/C_{60} fiber mat, which proves the homogeneous mixture of C_{60} in the fiber mat solution for electrospinning. The presence of a few beads in the cross-linked, electrospun, and pyrolyzed fiber mats has been illustrated in Figure 2h−j. The SEM images show that after pyrolysis at high temperatures, all the beads had undergone shrinkage, resulting in the formation of microbeads within the pyrolyzed sample. Additionally, a pyrolyzed SiOC fiber mat was prepared to study the comparison with SiOC/C_{60}, and its SEM images and XRF data have been shown in Figure S1. Some irregularities, such as more broken fibers in the SiOC fiber mat compared to the SiOC/C_{60} fiber mat, can be observed from the SEM images, which may have occurred due to the brittle nature caused by the high-temperature pyrolysis of the fiber mat.

The XRF spectra of the C_{60} powder, pyrolyzed PVP fiber mat, 4TTCS/C_{60} electrospun fiber mat, cross-linked fiber mat, and pyrolyzed SiOC/C_{60} fiber mat are shown in Figure 2k−o. The XRF data demonstrate the elemental analysis of the fiber mats, and all the elemental compositions are listed in Table S1. In the XRF of C_{60} powder (Figure 2k), there is only a single

distinct carbon peak, which signifies its high purity. Also, the pyrolyzed PVP contains only carbon and oxygen, which reveals that, during electrospinning, cross-linking, or pyrolysis processes, the fiber mats were not contaminated by any other means. The SiOC/C_{60} fiber mat contains a higher wt % of C compared to SiOC (Table S1), which confirms the presence of C_{60} fullerene inside the fibers.

The morphology of bulk C_{60} powder and SiOC/C_{60} fiber mat was investigated by TEM, as shown in Figure 3. The clusters of C_{60} fullerene, shown in Figure 3a,b, were investigated through the SAED pattern (Figure 3c), where the bright spots overlay concentric diffusive rings, which could be due to a truncated icosahedral structure.[32] The SAED pattern revealed the associated (111), (220), (222), (420), and (333) planes of C_{60} corresponding to the d-spacing of 8.2, 5.07, 4.2, 3.2, and 2.8 Å, respectively, of the face-centered cubic (fcc) lattice (powder diffraction file: 820505).[33] On the other hand, long fibers were observable in the TEM image of the C_{60}-embedded pyrolyzed SiOC fiber mat, as seen in Figure 3d−f, and the porosity within the fiber mat was visible in the HRTEM image, as seen in Figure 3g. Pores observed in HRTEM may have allowed the fibers used as the electrode material to sustain volume change and facilitate charge transfer at the electrode−electrolyte interface, which enhanced the

electrochemical storage capacity.[34] The SAED pattern of the SiOC/C_{60} fiber mat (Figure 3h) revealed that the fibers show similar crystallographic planes as those observed in C_{60} powder, proving the incorporation of C_{60} fullerene within the fibers (ICSD 74523). The concentric diffusive rings in the SAED pattern were not present, which could be due to the thermal instability of C_{60} fullerene when subjected to pyrolysis at 800 °C within the SiOC/C_{60} fiber mat. At this elevated temperature, the truncated icosahedral structure could have been broken, affecting the diffraction pattern.[35]

Raman spectroscopy analysis of the C_{60} powder, pyrolyzed fiber mat, and SiOC/C_{60} fiber mat provided the structural fingerprint and vibrational modes of the molecules, which are shown in Figure 4a. The peak for Raman shift at 1470 cm^{-1} for the C_{60} powder denotes the $A_g(2)$ pentagonal pinch mode.[36] Both the pyrolyzed PVP and the SiOC/C_{60} fiber mats have a D band at 1336 and 1330 cm^{-1}, along with a G band at 1598 and 1590 cm^{-1}, respectively.[11] The D band appeared due to the disorder-induced vibration of the carbon phase, while the G band represents the in-plane stretching of the sp^2 hybridized carbon.[37] Also, peaks at 1198 and 1481 cm^{-1} were observed for the SiOC/C_{60} fiber mat, which represent T and D″ bands, respectively. The T band represents sp^2–sp^3 (C–C and C=C) bonds, while the D″ band represents the presence of amorphous carbon due to the edges of the graphene layers, pores, and sp^3 hybridization.[38] In the SiOC/C_{60} fiber mat, the Raman peak of C_{60} powder at 1467 cm^{-1} is likely suppressed by the D″ peak from SiOC.

Figure 4b illustrates the FTIR results with characteristic absorption bands that explore the intricate bonding and molecular interactions within the fiber matrix for electrospun, cross-linked, and pyrolyzed SiOC/C_{60} fiber mats, along with pyrolyzed PVP. Electrospun and cross-linked 4-TTCS/C_{60} samples show different chemical characteristics at different wavenumbers, which have been listed in Table 1.

Table 1. FTIR Spectra of the Electrospun 4TTCS/C_{60} Fiber Mat

wavenumber (cm−1)	chemical group	reference
1648	C–O stretching	31,39
1598	Si–CH=CH$_2$ (C=C stretching)	31,40
1419	CH bending	31,39
1408	Si–CH$_3$ (C–H asymmetric bending)	31,40
1289	CH$_2$ wagging	31,39
1260	Si–CH$_3$ (C–H symmetric bending)	31,40
1070	Si–O–Si asymmetric stretching	31,40
1007	Si–CH=CH$_2$ (CH out-of-plane bending)	31,40
960	Si–CH=CH$_2$ (CH out-of-plane bending)	31,40
793	Si–CH$_3$ (Si–C deformation vibration)	31,41
746	Si–CH$_3$ (Si–C deformation vibration)	31,41
645	Si–CH$_3$ (Si–C stretching)	31,40
570	N–C = O bending	31,39

The observed reduction in the peak for Si–CH$_3$ and Si–CH=CH$_2$ in the cross-linked sample compared to the electrospun sample suggested that the cross-linking reaction took place at 160 °C. After pyrolysis at 800 °C, the SiOC/C_{60} fiber mat showed strong absorption at 1050 cm^{-1} (Si–O) and a very weaker absorption at 800 cm^{-1} (Si–C), while the pyrolyzed PVP did not have any absorption peak. This confirms the presence of more Si–O bonds compared with the Si–C bond in the SiOC/C_{60} fiber mat.

The XPS of the SiOC/C_{60} fiber mat was investigated to study surface characteristics, identify material constituents, and explore the chemical and electronic states of the sample. Figure 5a illustrates the XPS survey scan of the pyrolyzed SiOC/C_{60} fiber mat containing the peaks for O 1s, N 1s, C 1s, and Si 2p. Based on the elemental composition acquired from the XPS survey (Table S2), the SiOC/C_{60} fiber mat contains mostly C 1s (72.10 wt %), along with 16.55 wt % of O 1s and 9.09 wt % of Si 2p. Also, the pyrolyzed sample exhibited a small quantity of nitrogen (2.25 wt %), presumably originating from PVP. The high-resolution and curve-fitted XPS spectra for Si 2p, O 1s, and C 1s have been shown in Figure 5b–d, respectively. The Si 2p spectra in Figure 5b indicate the presence of SiCO$_3$ (103.4 eV)[31] and SiC$_2$O$_2$ (102.8 eV)[31] peaks. The deconvoluted O 1s spectra in Figure 5c show C=O (534.4 eV)[31] and O–Si (532.7 eV)[31] bonds. Figure 5d demonstrates the presence of C =O (287.2 eV),[31] C–O–Si (285 eV),[42] and C–C (284.6 eV)[43] bonds in the C 1s spectra.

Thermogravimetric analysis (TGA) was also conducted in flowing air to estimate the burning temperature of C_{60} and to understand the thermal stability of the pyrolyzed SiOC/C_{60} fiber mat in terms of weight. As shown in Figure S2, the C_{60} powder oxidized at around 670 °C, while Bhandavat and Singh et al. stated that SiOC barely started oxidizing at 1000 °C.[12] Figure S2 also shows that at 1000 °C, SiOC/C_{60} loses ∼13% of its weight. Therefore, we can assume that approximately 13 wt % of C_{60} is present in the pyrolyzed SiOC/C_{60} fiber mat.

The C_{60} on Cu foil-pyrolyzed PVP fiber mat and pyrolyzed SiOC/C_{60} fiber mat were used as electrodes to analyze the electrochemical energy storage capability in lithium half-cells. The galvanostatic charge–discharge profile for the first three cycles, shown in Figure 6a,c,e, was used to investigate the Li$^+$ electrochemical reactions at various potentials. The differential capacity curves, shown in Figure 6b,d,f, derived from the GCD profile provided enhanced clarity of the plateaus present in the GCD profile by transforming them into distinct peaks. At a current density of 50 mA g^{-1}, the charge–discharge profile of samples showed an irreversible capacity decay in the first cycle. Among others, C_{60} on Cu foil showed the highest capacity decay in the first cycle with an initial discharge capacity of 2139.90 mA h g^{-1} and a charge capacity of only 150.58 mA h g^{-1}, corresponding to a very low Coulombic efficiency of 7.04%. The pyrolyzed PVP fiber mat showed 904.62 and 552.75 mA h g^{-1}, respectively, for discharge and charge capacity in the first cycle, demonstrating a comparatively higher Coulombic efficiency of over 61%. The SiOC/C_{60} fiber mat showed a first-cycle discharge capacity of 1850 mA h g^{-1} and a charge capacity of 1211.97 mA h g^{-1}, with the highest Coulombic efficiency of 65.51%.

The differential capacity curve for the C_{60} Cu foil (Figure 6b) had reduction peaks at 1.06, 1.60, and 1.92 V, which represents lithiation of C_{60}, and 2.15 V in the first cycle represents electrolyte additive decomposition and SEI formation.[44,45] The differential capacity curve of the pyrolyzed PVP fiber mat showed reduction peaks at 0.24 V, which may be attributed to lithiation, and 0.91 V, which may be referred to SEI layer formation, and oxidization peaks at 0.40 and 1.07 V in Figure 6d refer to delithiation. The SiOC/C_{60} fiber mat showed reduction peaks at 0.09, 0.20, 0.73, and 1.01 V, with oxidization peaks at 0.08, 0.40, and 1.05 V in the first cycle in Figure 6f. The reduction peak at 0.09 V indicates the lithium
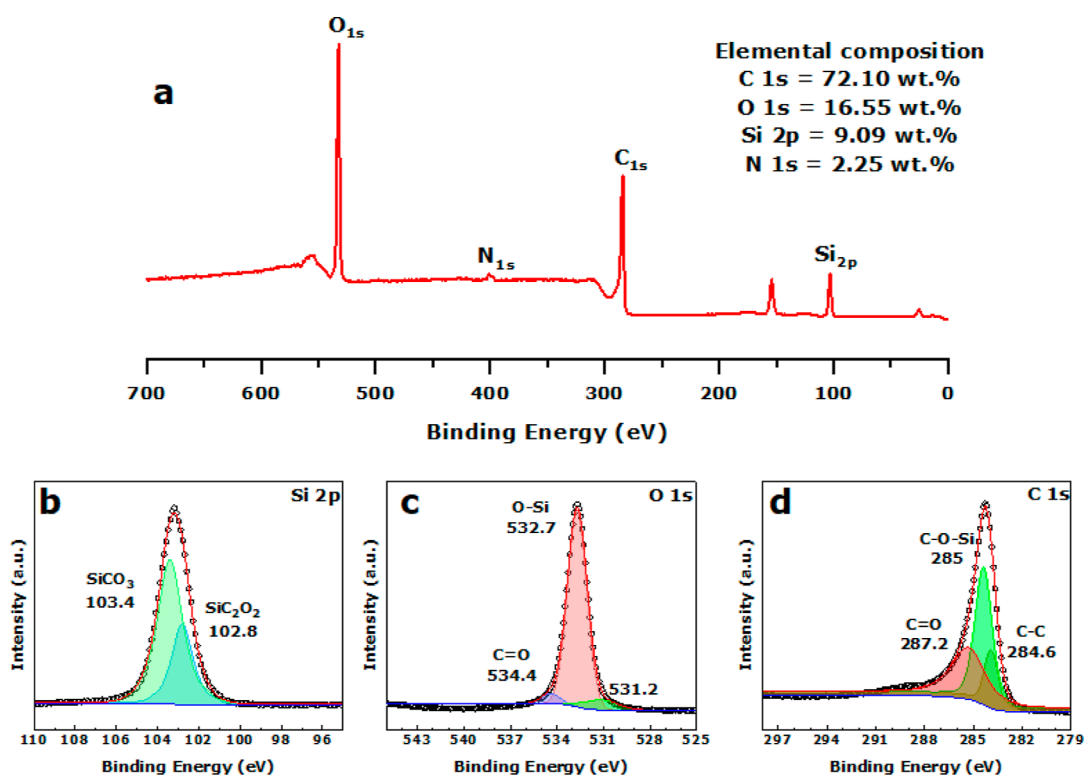
Figure 5. (a) XPS survey scan of the SiOC/C_{60} fiber mat representing the presence of individual elements; high-resolution XPS spectra of (b) Si 2p, (c) O 1s, and (d) C 1s obtained from the SiOC/C_{60} fiber mat showing the bonding states of the Si, C, and O in the SiOC matrix.
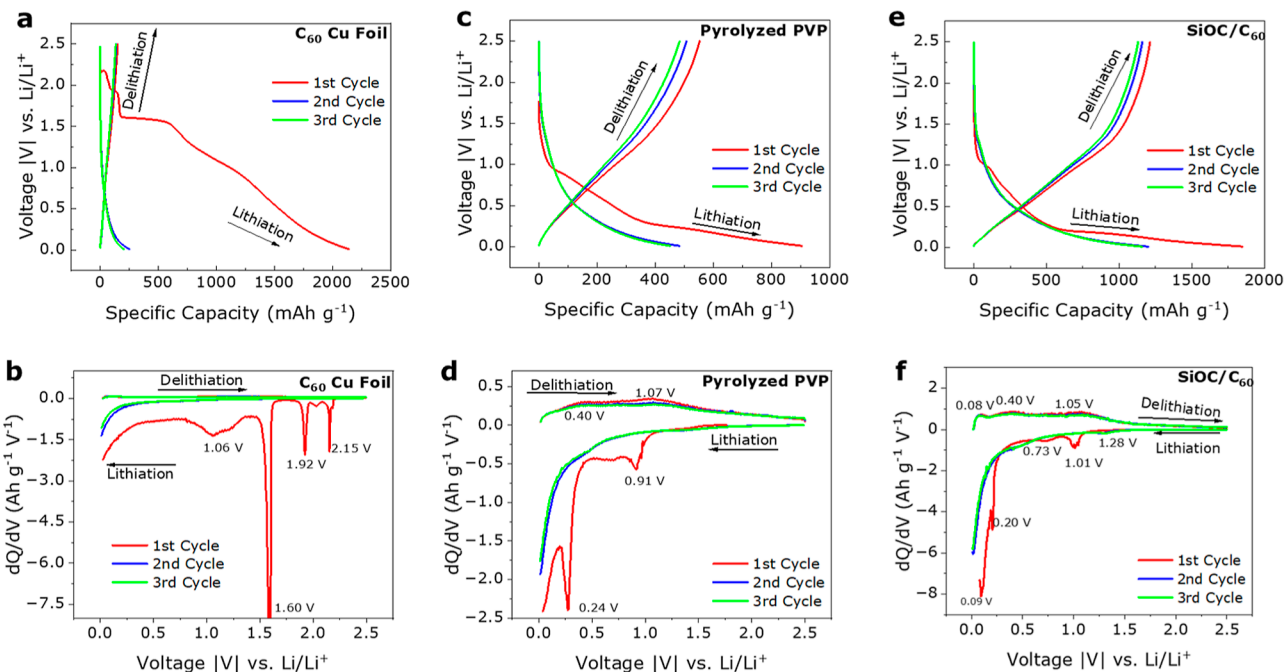

Figure 6. Electrochemical performances of the samples in Li-ion half-cell setup: (a,c,e) GCD profiles of the C_{60}, pyrolyzed PVP, and SiOC/C_{60} electrodes, respectively; (b,d,f) differential capacity curves of the C_{60}, pyrolyzed PVP, and SiOC/C_{60} electrodes, respectively, derived from the GCD profiles, providing information regarding reactions taking place at different voltages.

interaction in the graphitic carbon of the fiber mat.[12,46] The reduction peak at 0.20 V indicates Li$^+$-insertion into the $Si_xO_yC_z$ amorphous carbon phases.[10,47,48] The reduction peak at 0.73 V was attributed to the SEI formation due to the LiPF$_6$-based electrolyte and was present only in the first cycle.[12] The reduction peak at 1.01 V was very similar to the broad 1.06 V

peak of the C_{60} Cu foil sample, which proves the participation of C_{60} fullerene in the lithiation process. Also, the oxidation peaks at 0.08, 0.40, and 1.05 V in all three cycles indicate the delithiation process.

A rate capability test of the half-cells, shown in Figure 7, was investigated at 50, 800, and 1600 mA g^{-1} for 50 cycles each
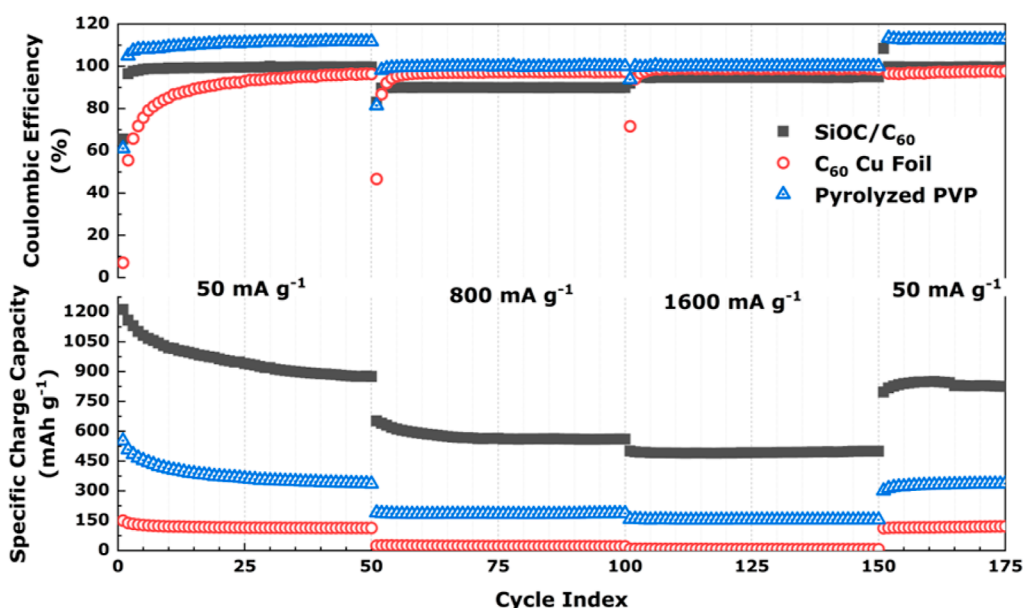
Figure 7. Rate capability test performed for the C_{60}, pyrolyzed PVP, and SiOC/C_{60} electrodes showing superior capacity and efficiency for the SiOC/C_{60} cell.

and returned to 50 mA g^{-1} for 100 cycles. The C_{60} Cu foil half-cell was stabilized at 113 mA h g^{-1} at 50 mA g^{-1} after 50 cycles and performed very poorly at both 800 and 1600 mA g^{-1} for the next 100 cycles. However, it recovered to 124 mA h g^{-1} at a 50 mA g^{-1} current density for the last 25 cycles. The half-cell with the pyrolyzed PVP fiber mat electrode showed a charge capacity of 335 mA h g^{-1} at 50 mA g^{-1} current density after 50 cycles, 187 mA h g^{-1} at 800 mA g^{-1} current density after the next 50 cycles, and only 154 mA h g^{-1} at 1600 mA g^{-1} current density after the next 50 cycles and recovered to 336 mA h g^{-1} at 50 mA g^{-1} current density for the last 25 cycles. The cycling stability test of the SiOC fiber mat, shown in Figure S3, exhibited the first cycle charge capacity of 474 mA h g^{-1} at a current density of 50 mA g^{-1}, which stabilized at 312 mA h g^{-1} after 50 cycles. The SiOC/C_{60} fiber mat performed exceptionally well with an initial charge capacity of 1211 mA h g^{-1}, which dropped to 875 mA h g^{-1} after 50 cycles at 50 mA g^{-1} with a retention capacity of more than 96%. After 50 cycles at 800 mA g^{-1} current density, the performance of the half-cell demonstrated stabilized performance at 560 mA h g^{-1} with a Coulombic efficiency of over 97%. The SiOC/C_{60} half-cell showed an almost 500 mA h g^{-1} specific charge capacity after 50 cycles, even at a higher current density (1600 mA g^{-1}), with almost 99% retention capacity. In the last 25 cycles at 50 mA h g^{-1}, the cell showed a constant capacity of 825 mA h g^{-1} with more than 99% retention capacity. Also, the cycling stability of SiOC/C_{60} powder was investigated to understand the electrochemical performance compared with the fiber mat form. The SiOC/C_{60} powder was synthesized using a method similar to and under exact conditions to the fiber mat, only without the electrospinning step. Then, the powders were used to prepare an electrode on Cu foil, following conditions similar to those of the C_{60} Cu foil electrode. The powder form of SiOC/C_{60} demonstrates a low overall specific capacity compared to the fiber mat form, as shown in Figure S4.

The performance comparison of all of the half-cells of this study has been listed in Table 2.

In addition, the electrochemical performance comparison of the polymer-derived SiOC fiber mat (without the C_{60})

Table 2. Summary of the Electrochemical Performance of This Study

half-cells	current density (mA g^{-1})	first cycle sp. charge capacity (mA h g^{-1})	first cycle coulombic efficiency (%)	specific charge capacity at 50th cycle (mA h g^{-1})
C_{60} Cu foil	50	150	07	113
Py PVP fiber mat	50	552	61	335
SiOC fiber mat	50	474	64	312
SiOC/C_{60} fiber mat	50	1211	65	875

electrode and SiOC/C_{60} fiber mat is presented in Table S3, and the SiOC/C_{60} fiber mat exhibited superior performance compared to other studies in terms of both capacity and cyclability.

This superior performance of SiOC/C_{60} may have resulted from the presence of C_{60} and related graphitic or diamond-like carbon formed in SiOC. During the cross-linking and pyrolysis of the fiber mat, the embedded C_{60} fullerenes also undergo low- and high-temperature heat treatment, which may result in favorable structural changes as reported in previous studies, which increase the conductivity of C_{60}, leading to better overall electrode performance.[49−51] Also, these structural changes of C_{60} can sometimes lead to the formation of few-layer graphite and diamond-like carbon forms,[52] which contributed to the content of free carbons in the fiber mat. Hence, during high-temperature pyrolysis, this carbon-rich SiOC fiber mat undergoes delayed SiOC phase separation and crystallization into SiO_2 and SiC, which provides additional Li-ion storing sites, increased structural stability, and decreased electrical resistivity.[53,54] Previously reported SiOC ceramic powder derived from the same or similar polysiloxane precursors exhibited insulating behavior with a conductivity of $\sim 10^{-12}$ S cm^{-1}.[12,55] However, the reported conductivity of carbon-rich SiOC composite papers was in the range of 0.02−1.05 S cm^{-1}.[10] The fiber mat form of pyrolyzed PVP and SiOC/C_{60} in this study exhibited a conductivity of 6.25 S and 14.28 S cm^{-1},
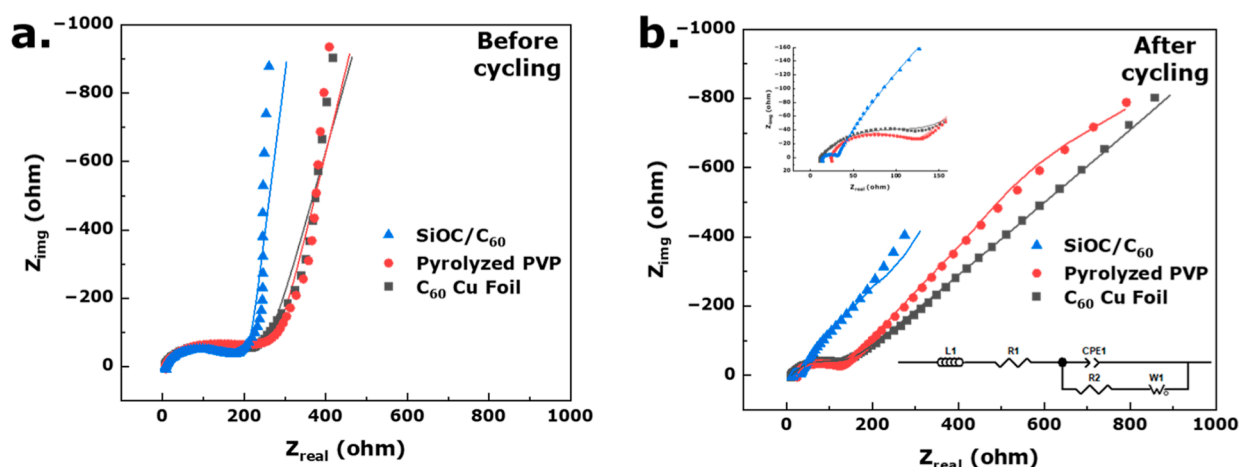
Figure 8. Fitted Nyquist plot for C_{60} Cu foil, pyrolyzed PVP, and SiOC/C_{60} cells (a) before and (b) after cycling demonstrates the lowest resistance for the SiOC/C_{60} cell.
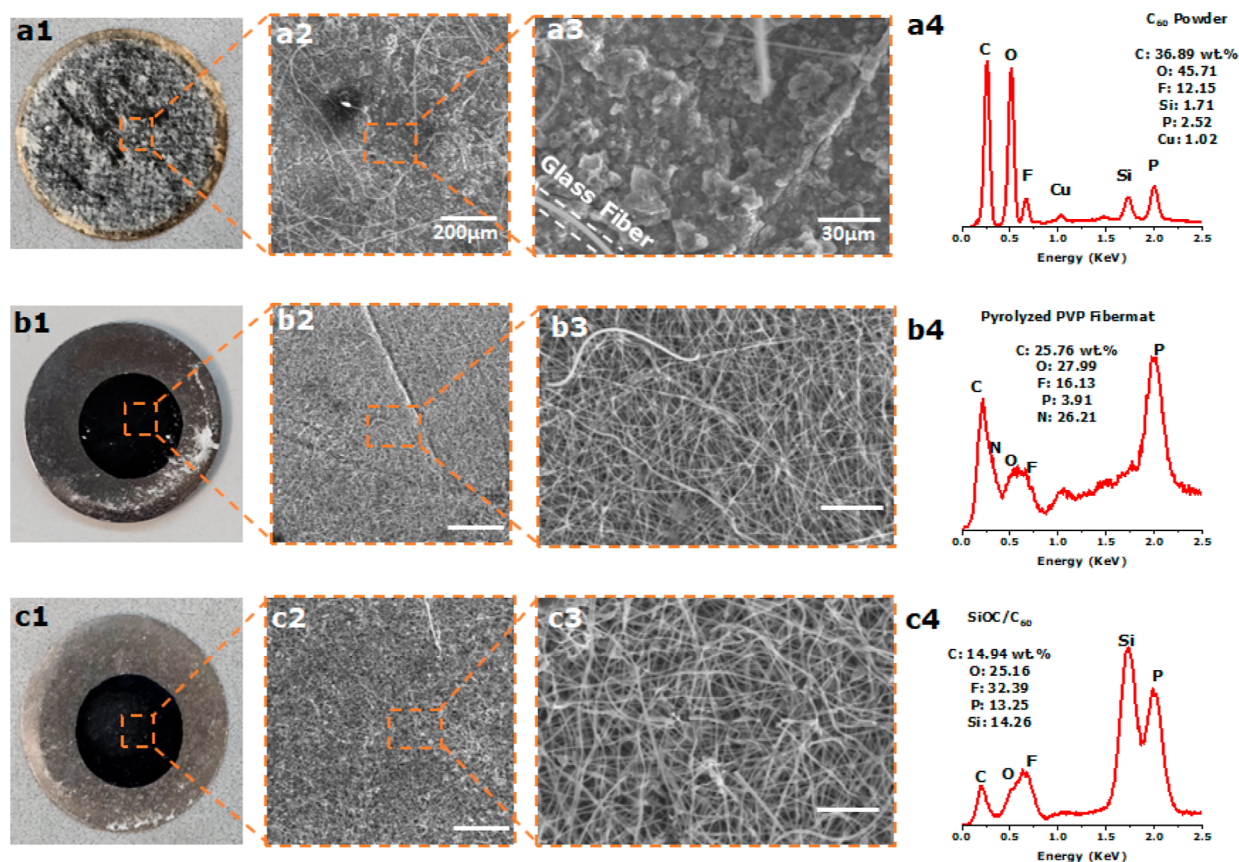

Figure 9. Camera pictures of postcycled (a1−c1) C_{60} Cu foil, pyrolyzed PVP fiber mat, SiOC/C_{60} fiber mat electrodes, and their corresponding (a2−c2) SEM images (scale: 200 μm) and (a3−c3) high-magnification SEM images (scale: 30 μm) show the change in electrodes after a long cycling process; and (a4−c4) corresponding XRF spectra (all the elemental composition values are presented in wt %) reveal the elemental composition of the spent electrodes.

respectively, which is an improvement compared to other studies.[53,56]

To understand the kinetic behavior of the electrodes, electrochemical impedance spectroscopy (EIS) of half-cells both before and after cycling was performed. The Nyquist plot in Figure 8a,b was fitted with an equivalent Randles circuit using Zview software (v 3.2b, Copyright Scribner Associates, Inc., Southern Pines, NC, USA). The Nyquist plot illustrated an inductive loop in the high-frequency zone, which could be due to the measurement system or cell geometry and windings. The internal ohmic resistance, R_{ohm}, caused by active material, electrolyte, and electrical contacts, was common to all cells and intercepted the real impedance axis. The semicircular curve in the high-frequency stage denotes charge transfer impedance, which arises from the electrolyte and the electrode interface contact.[57,58] The SEI formation and charge transfer were not distinguishable in the plot; hence, CPE_{dl} and R_{CT} elements were fitted in parallel. The sloping line in the low-frequency

range of the Nyquist plot indicated the solid-state diffusion and was fitted with the Warburg element.[59] The obtained fitted EIS data are listed in Table S4 for before and after cycling, respectively. Also, the equivalent circuit is shown in the inset of Figure 8b. The nomenclature of the EIS symbols has been explained in the Supporting Information. Comparing Tables S4 and S5, the R_{ohm} and $W-R$ values increase after cycling compared to pristine cells. The increase in the ohmic resistance or R_{ohm} value, also known as electrolyte resistance, is due to the reduction in the count of accessible sites for Li ions, electrolyte substance decomposition (such as PF_6^- and EC/DMC), or an elevation of concentration of organic species in the electrolyte solution which impede the mobility of Li-ions.[59−61] The $W-R$ value or Warburg resistance may have increased due to solid- and liquid-state diffusion. Despite the fact of additional sites for Li-ion diffusion and the reduction in diffusion length due to the presence of the nanomaterial, resistances may persist because of the nonuniformity in active material size in the electrode.[59,62] On the other hand, R_{CT} values decrease after cycling compared to pristine cells, which may have occurred due to the increase in internal resistance and capacity decay of the half-cells over the cycling period.[63] The tabulated data after cycling show that R_{ohm} is 11.56 for the C_{60} Cu foil electrode, and for the pyrolyzed PVP sample, R_{ohm} (= 23.26) is the highest. However, for the SiOC/C_{60} cycled electrode, R_{ohm} had the lowest value of 10.07 while maintaining the lowest CPE_{dl} (N) and lowest R_{CT} of only 25.78 compared to cycled C_{60} Cu foil and cycled pyrolyzed PVP R_{CT} values of 128.4 and 96.84, respectively. Additionally, the spent SiOC/C_{60} electrode boasts a low $W-R$ value compared to C_{60} Cu foil. The deviation of $W-P$ values from the ideal condition indicates the existence of other processes beyond solid-state diffusion, such as migration and liquid/electrolyte phase diffusion.[59]

All of the half-cells were disassembled in an inert (Ar) environment after cycling. The postcycling analysis of the electrodes included camera pictures, SEM, and XRF character- ization techniques, as shown in Figure 9. The white layer in Figure 9a1 and the long fibers in Figure 9a2,a3 indicate the presence of glass fibers on the C_{60} Cu foil electrode from the separator. The white layer of the glass separator was not present in the pyrolyzed PVP fiber mat (Figure 9b1) and SiOC/C_{60} fiber mat (Figure 9c1). The high-magnification SEM image in Figure 9a3 compared to that in Figure 2f demonstrates that the large C_{60} clusters have broken down into smaller fragments due to the lithium-ion intercalation. The diameter distribution plots in Figure S5a−d were extrapolated from SEM images of Figure 2g for precycle and Figure 9b2,b3 for postcycle pyrolyzed PVP and Figure 2j for the precycle and Figure 9c2,c3 for the postcycle SiOC/C_{60} fiber mat electrode. In the pristine condition, the average fiber diameter for pyrolyzed PVP was found to be approximately 0.6−0.8 μm (Figure S5a), and the mean diameter for the SiOC/C_{60} fiber mat was around 1.0−1.4 μm (Figure S5c). After a long cycling process, the average diameter of the fibers was found to be around 0.8−0.9 μm (Figure S5b) and 1.6−2.0 μm (Figure S5d) for pyrolyzed PVP and SiOC/C_{60} fiber mat, respectively, which indicates the diameter increase of approximately 40%. Due to the presence of interfiber void spaces, the increase in fiber diameter could not exert any major impact on the overall volume change of the electrode.

The qualitative elemental analysis was conducted using the XRF technique on the spent electrodes. The resulting data are plotted in Figure 9a4−c4, and the elemental composition is detailed in Table S6. All of the electrodes exhibited characteristic peaks of C and O, suggesting the presence of carbon and oxygen after cycling. Additionally, peaks for F and P were also discernible due to the use of the $LiPF_6$ electrolyte. The copper peak observed in Figure 9a4 may have arisen due to the C_{60} coating on Cu foil, and the presence of glass fibers from the separator may have resulted in the silicon peak.[30] Also, the absence of a glass separator on the SiOC/C_{60} spent electrode fiber mat indicates that the silicon peak observed in the XRF spectrum (Figure 9c4) originated from the silicon element present in the PDC precursor.

4. CONCLUSIONS

In summary, the fabrication of nonwoven fiber mats of C_{60} buckminsterfullerene-reinforced SiOC is realized by dissolving C_{60} nanopowders in a liquid-phase hybrid precursor of TTCS and PVP, followed by electrospinning and pyrolysis in Ar gas. The mass fraction of C_{60} in the polymer precursor was set at 5 wt %. The pyrolyzed composite fibers produced had an average diameter of approximately 1.2 μm. The presence of C_{60} in the fiber mat was mainly confirmed by the use of TEM electron diffraction. Also, the TGA mass loss analysis of the SiOC/C_{60} fiber mat and C_{60} and comparison with neat SiOC suggested approximately 13 wt % loading of carbon forms from C_{60} in the SiOC/C_{60} pyrolyzed fiber mat. The lithium half-cell compris- ing of SiOC/C_{60} fiber mat working electrode maintained a specific charge capacity of 825 mA h g^{-1} after 175 cycles, which was more than 2 and 6 times that of neat carbonized PVP fiber and neat C_{60} electrodes, respectively. Significant improvement in Li-ion charge capacity, rate capability, and stability for the SiOC/C_{60} fiber mat over SiOC and C_{60} electrodes is attributed to high electrical conductivity because of high free carbon content (formation of percolation networks) and a robust Si−O−C mixed bond network structure that offered large sites for active Li^+ and fiber morphology that improved wetting by the electrolyte and provided smooth channels for ion transportation to/from the electrolyte/electrode interface.

■ ASSOCIATED CONTENT

ⓢ Supporting Information

The Supporting Information is available free of charge at https://pubs.acs.org/doi/10.1021/acsomega.4c04224.

> SEM and XRF spectra of the SiOC fiber mat, elemental composition of the pristine half-cell electrode deter- mined by XRF and XPS, TGA data, cycling stability and Coulombic efficiency comparison for SiOC/C_{60} and SiOC fiber mat electrodes, cycling stability and Coulombic efficiency comparison for SiOC/C_{60} powder on the Cu foil electrode with fiber mat form, electrochemical performance comparison of different SiOC fiber mat anodes for LIBs, circuit-fitted results from EIS experiments before cycling, circuit-fitted results from EIS experiments after cycling, diameter distribution plot of precycle and postcycle fiber mats, and elemental composition of the spent half-cell electrodes determined by XRF (PDF)

■ AUTHOR INFORMATION

Corresponding Author

Gurpreet Singh − *Department of Mechanical and Nuclear Engineering, Kansas State University, Manhattan, Kansas*

66506, United States; ● orcid.org/0000-0003-2126-9204;
Email: gurpreet@ksu.edu

Authors

Arijit Roy − Department of Mechanical and Nuclear
Engineering, Kansas State University, Manhattan, Kansas
66506, United States; ● orcid.org/0009-0004-8026-2330
Shakir Bin Mujib − Department of Mechanical and Nuclear
Engineering, Kansas State University, Manhattan, Kansas
66506, United States; ● orcid.org/0000-0002-6699-420X

Complete contact information is available at:
https://pubs.acs.org/10.1021/acsomega.4c04224

Author Contributions

Conceptualization: G.S.; methodology: G.S., A.R., and S.B.M.;
Cu foil and fiber mat electrode preparation: A.R; SEM, XRF,
TEM, Raman, and XPS: A.R. and S.B.M.; FTIR: A.R.; cell
assembly, data acquisition, GCD, CV, differential capacity, EIS:
A.R.; postcycling analysis: A.R. and S.B.M.; resources: G.S.;
data curation: A.R.; writing-original draft preparation: A.R. and
S.B.M.; writing-review and editing: G.S.; visualization: A.R.;
supervision: G.S.; funding acquisition: G.S. All authors have
read and agreed to the published version of the manuscript.

Notes

The authors declare no competing financial interest.

■ ACKNOWLEDGMENTS

■ REFERENCES

(1) Saha, A.; Raj, R.; Williamson, D. L. A Model for the
Nanodomains in Polymer-Derived SiCO. J. Am. Ceram. Soc. 2006,
89 (7), 2188−2195.
(2) Mujib, S. B.; Singh, G. Polymer derived SiOC and SiCN
ceramics for electrochemical energy storage: A perspective. Int. J.
Ceram. Eng. Sci. 2022, 4 (1), 4−9.
(3) Loughney, P. A.; Mujib, S. B.; Pruyn, T. L.; Singh, G.; Lu, K.;
Doan-Nguyen, V. Enhancing organosilicon polymer-derived ceramic
properties. J. Appl. Phys. 2022, 132 (7), 070901.
(4) Fukui, H.; Nakata, N.; Dokko, K.; Takemura, B.; Ohsuka, H.;
Hino, T.; Kanamura, K. Lithiation and Delithiation of Silicon
Oxycarbide Single Particles with a Unique Microstructure. ACS
Appl. Mater. Interfaces 2011, 3 (7), 2318−2322.
(5) Fukui, H.; Ohsuka, H.; Hino, T.; Kanamura, K. A Si-O-C
Composite Anode: High Capability and Proposed Mechanism of
Lithium Storage Associated with Microstructural Characteristics. ACS
Appl. Mater. Interfaces 2010, 2 (4), 998−1008.
(6) Dibandjo, P.; Graczyk-Zajac, M.; Riedel, R.; Pradeep, V. S.;
Soraru, G. D. Lithium insertion into dense and porous carbon-rich
polymer-derived SiOC ceramics. J. Eur. Ceram. Soc. 2012, 32 (10),
2495−2503.
(7) Bhandavat, R.; Pei, Z.; Singh, G. Polymer-derived ceramics as
anode material for rechargeable Li-ion batteries: a review. Nanomater.
Energy 2012, 1 (6), 324−337.

(8) Wen, Q.; Qu, F.; Yu, Z.; Graczyk-Zajac, M.; Xiong, X.; Riedel, R.
Si-based polymer-derived ceramics for energy conversion and storage.
J. Adv. Ceram. 2022, 11 (2), 197−246.
(9) Sujith, R.; Gangadhar, J.; Greenough, M.; Bordia, R. K.; Panda,
D. K. A review of silicon oxycarbide ceramics as next generation
anode materials for lithium-ion batteries and other electrochemical
applications. J. Mater. Chem. A 2023, 11 (38), 20324−20348.
(10) David, L.; Bhandavat, R.; Barrera, U.; Singh, G. Silicon
oxycarbide glass-graphene composite paper electrode for long-cycle
lithium-ion batteries. Nat. Commun. 2016, 7 (1), 10998.
(11) Dey, S.; Mujib, S. B.; Singh, G. Enhanced Li-Ion Rate
Capability and Stable Efficiency Enabled by MoSe2 Nanosheets in
Polymer-Derived Silicon Oxycarbide Fiber Electrodes. Nanomaterials
2022, 12 (3), 553.
(12) Bhandavat, R.; Singh, G. Stable and Efficient Li-Ion Battery
Anodes Prepared from Polymer-Derived Silicon Oxycarbide-Carbon
Nanotube Shell/Core Composites. J. Phys. Chem. C 2013, 117 (23),
11899−11905.
(13) Bhandavat, R.; Singh, G. Improved Electrochemical Capacity of
Precursor-Derived Si(B)CN-Carbon Nanotube Composite as Li-Ion
Battery Anode. ACS Appl. Mater. Interfaces 2012, 4 (10), 5092−5097.
(14) Kaspar, J.; Terzioglu, C.; Ionescu, E.; Graczyk-Zajac, M.; Hapis,
S.; Kleebe, H.-J.; Riedel, R. Stable SiOC/Sn Nanocomposite Anodes
for Lithium-Ion Batteries with Outstanding Cycling Stability. Adv.
Funct. Mater. 2014, 24 (26), 4097−4104.
(15) David, L.; Asok, D.; Singh, G. Synthesis and Extreme Rate
Capability of Si-Al-C-N Functionalized Carbon Nanotube Spray-on
Coatings as Li-Ion Battery Electrode. ACS Appl. Mater. Interfaces
2014, 6 (18), 16056−16064.
(16) Kolathodi, M. S.; David, L.; Abass, M. A.; Singh, G.
Polysiloxane-functionalized graphene oxide paper: pyrolysis and
performance as a Li-ion battery and supercapacitor electrode. RSC
Adv. 2016, 6 (78), 74323−74331.
(17) Jella, G.; Panda, D. K.; Sapkota, N.; Greenough, M.; Datta, S.
P.; Rao, A. M.; Sujith, R.; Bordia, R. K. Electrochemical Performance
of Polymer-Derived Silicon-Oxycarbide/Graphene Nanoplatelet
Composites for High-Performance Li-Ion Batteries. ACS Appl.
Mater. Interfaces 2023, 15 (25), 30039−30051.
(18) Feng, Q.; Xu, C.; Xie, X.; Liao, N. Enabling high performance
all-solid-state thin films microbatteries with silicon oxycarbide/
lithium-metal composites anodes. Surf. Interfaces 2024, 44, 103759.
(19) Chabre, Y.; Djurado, D.; Armand, M.; Romanow, W. R.;
Coustel, N.; McCauley, J. P., Jr.; Fischer, J. E.; Smith, A. B., III.
Electrochemical intercalation of lithium into solid fullerene C60. J.
Am. Chem. Soc. 1992, 114 (2), 764−766.
(20) Yoshiyama, N.; Endo, H.; Yamamoto, H. Electrochemical
doping of alkali metals into C60 thin film. J. Supercond. 1995, 8 (1),
5−8.
(21) Li, Z.; Smeu, M.; Rives, A.; Maraval, V.; Chauvin, R.; Ratner,
M. A.; Borguet, E. Towards graphyne molecular electronics. Nat.
Commun. 2015, 6 (1), 6321.
(22) Wakamatsu, K.; Sekihara, A.; Yamaguchi, Y.; Matsushima, R.;
Matsumura, D.; Kuila, T.; Yoshikawa, H. Electron Storage Perform-
ance of Hybrid Materials Comprising Polyoxometalates and Carbon
Nanohorns as Cathode-Active Materials. Batteries Supercaps 2023, 6
(1), No. e202200385.
(23) Kim, I.-S.; Shim, C.-E.; Kim, S. W.; Lee, C.-S.; Kwon, J.; Byun,
K.-E.; Jeong, U. Amorphous Carbon Films for Electronic
Applications. Adv. Mater. 2023, 35 (43), 2204912.
(24) Yin, L.; Cho, J.; Kim, S. J.; Jeon, I.; Jeon, I.; Park, M.; Park, M.;
Jeong, S.-Y.; Lee, D. H.; Seo, D.-H.; Cho, C.-R. Abnormally High-
Lithium Storage in Pure Crystalline C60 Nanoparticles. Adv. Mater.
2021, 33 (43), 2104763.
(25) Jiang, Z.; Zhao, Y.; Lu, X.; Xie, J. Fullerenes for rechargeable
battery applications: Recent developments and future perspectives. J.
Energy Chem. 2021, 55, 70−79.
(26) Yazami, R.; Cherigui, A. The Electrochemical Behaviour of
Fullerenes in Liquid Electrolyte. Mol. Cryst. Liq. Cryst. Sci. Technol.,
Sect. A 1994, 244 (1), 209−214.

(27) Seger, L.; Wen, L. Q.; Schlenoff, J. B. Prospects for Using C 60 and C 70 in Lithium Batteries. *J. Electrochem. Soc.* **1991**, *138* (12), L81.

(28) Tan, Z.; Ni, K.; Chen, G.; Zeng, W.; Tao, Z.; Ikram, M.; Zhang, Q.; Wang, H.; Sun, L.; Zhu, X.; Wu, X.; Ji, H.; Ruoff, R. S.; Zhu, Y. Incorporating Pyrrolic and Pyridinic Nitrogen into a Porous Carbon made from C60 Molecules to Obtain Superior Energy Storage. *Adv. Mater.* **2017**, *29* (8), 1603414.

(29) Park, J.; Joo, S. H.; Kim, Y.-J.; Park, J. H.; Kwak, S. K.; Ahn, S.; Kang, S. J. Organic Semiconductor Cocrystal for Highly Conductive Lithium Host Electrode. *Adv. Funct. Mater.* **2019**, *29* (32), 1902888.

(30) Dey, S.; Manjunath, K.; Zak, A.; Singh, G. WS2 Nanotube-Embedded SiOC Fibermat Electrodes for Sodium-Ion Batteries. *ACS Omega* **2023**, *8* (11), 10126−10138.

(31) Ren, Z.; Gervais, C.; Singh, G. Fabrication and characterization of silicon oxycarbide fibre-mats via electrospinning for high temperature applications. *RSC Adv.* **2020**, *10* (63), 38446−38455.

(32) Kostant, B. Structure of the truncated icosahedron (such as fullerene or viral coatings) and a 60-element conjugacy class in PSl (2, 11). *Proc. Natl. Acad. Sci. U.S.A.* **1994**, *91* (24), 11714−11717.

(33) Dorset, D. L.; McCourt, M. P. Disorder and the molecular packing of C60 Buckminsterfullerene: a direct electron-crystallographic analysis. *Acta Crystallogr., Sect. A: Found. Crystallogr.* **1994**, *50* (3), 344−351.

(34) Ji, L.; Lin, Z.; Medford, A. J.; Zhang, X. Porous carbon nanofibers from electrospun polyacrylonitrile/SiO2 composites as an energy storage material. *Carbon* **2009**, *47* (14), 3346−3354.

(35) Nikonova, R. M.; Lad'yanov, V. I.; Rekhviashvili, S. S.; Pskhu, A. V. Thermal Stability of C60 and C70 Fullerites. *High Temp.* **2021**, *59* (2−6), 179−183.

(36) Bethune, D.; Meijer, G.; Tang, W. C.; Rosen, H. J.; Golden, W. G.; Seki, H.; Brown, C.; de Vries, M. S. Vibrational Raman and infrared spectra of chromatographically separated C60 and C70 fullerene clusters. *Chem. Phys. Lett.* **1991**, *179*, 181−186.

(37) Dong, B.; Han, Y.; Wang, T.; Lei, Z.; Chen, Y.; Wang, F.; Abadikhah, H.; Khan, S. A.; Hao, L.; Xu, X.; Cao, R.; Yin, L.; Agathopoulos, S. Hard SiOC Microbeads as a High-Performance Lithium-Ion Battery Anode. *ACS Appl. Energy Mater.* **2020**, *3* (10), 10183−10191.

(38) Mera, G.; Navrotsky, A.; Sen, S.; Kleebe, H.-J.; Riedel, R. Polymer-derived SiCN and SiOC ceramics - structure and energetics at the nanoscale. *J. Mater. Chem. A* **2013**, *1* (12), 3826−3836.

(39) Rahma, A.; Munir, M. M.; Khairurrijal; Prasetyo, A.; Suendo, V.; Rachmawati, H. Intermolecular Interactions and the Release Pattern of Electrospun Curcumin-Polyvinyl(pyrrolidone) Fiber. *Biol. Pharm. Bull.* **2016**, *39* (2), 163−173.

(40) Nyczyk, A.; Paluszkiewicz, C.; Pyda, A.; Hasik, M. Preceramic polysiloxane networks obtained by hydrosilylation of 1,3,5,7-tetravinyl-1,3,5,7-tetramethylcyclotetrasiloxane. *Spectrochim. Acta, Part A* **2011**, *79* (4), 801−808.

(41) Zhang, Y.; Li, Y.; Shao, J.; Zou, C. Fabrication of superhydrophobic fluorine-free films on cotton fabrics through plasma-induced grafting polymerization of 1,3,5,7-tetravinyl-1,3,5,7-tetramethylcyclotetrasiloxane. *Surf. Coat. Technol.* **2015**, *276*, 16−22.

(42) Zeng, S.; Feng, W.; Peng, S.; Teng, Z.; Chen, C.; Zhang, H.; Peng, S. Dual-functional SiOC ceramics coating modified carbon fibers with enhanced microwave absorption performance. *RSC Adv.* **2019**, *9* (53), 30685−30692.

(43) Han, M.; Yin, X.; Duan, W.; Ren, S.; Zhang, L.; Cheng, L. Hierarchical graphene/SiC nanowire networks in polymer-derived ceramics with enhanced electromagnetic wave absorbing capability. *J. Eur. Ceram. Soc.* **2016**, *36* (11), 2695−2703.

(44) Yin, L.; Yang, D.; Jeon, I.; Seo, J.; Chen, H.; Kang, M. S.; Park, M.; Cho, C.-R. Enhancing Li-Ion Battery Anodes: Synthesis, Characterization, and Electrochemical Performance of Crystalline C60 Nanorods with Controlled Morphology and Phase Transition. *ACS Appl. Mater. Interfaces* **2024**, *16* (15), 18800−18811.

(45) Shan, C.; Yen, H.-J.; Wu, K.; Lin, Q.; Zhou, M.; Guo, X.; Wu, D.; Zhang, H.; Wu, G.; Wang, H.-L. Functionalized fullerenes for

highly efficient lithium ion storage: Structure-property-performance correlation with energy implications. *Nano Energy* **2017**, *40*, 327−335.

(46) Graczyk-Zajac, M.; Toma, L.; Fasel, C.; Riedel, R. Carbon-rich SiOC anodes for lithium-ion batteries: Part I. Influence of material UV-pre-treatment on high power properties. *Solid State Ionics* **2012**, *225*, 522−526.

(47) Liu, X.; Zheng, M.-C.; Xie, K. Mechanism of lithium storage in Si-O-C composite anodes. *J. Power Sources* **2011**, *196* (24), 10667−10672.

(48) Mujib, S. B.; Ribot, F.; Gervais, C.; Singh, G. Self-supporting carbon-rich SiOC ceramic electrodes for lithium-ion batteries and aqueous supercapacitors. *RSC Adv.* **2021**, *11* (56), 35440−35454.

(49) Miyazawa, K.; Minato, J.; Fujino, M.; Suga, T. Structural investigation of heat-treated fullerene nanotubes and nanowhiskers. *Diamond Relat. Mater.* **2006**, *15* (4−8), 1143−1146.

(50) Miyazawa, K. i.; Minato, J.-i.; Zhou, H.; Taguchi, T.; Honma, I.; Suga, T. Structure and electrical properties of heat-treated fullerene nanowhiskers as potential energy device materials. *J. Eur. Ceram. Soc.* **2006**, *26* (4−5), 429−434.

(51) Jayatissa, A. H.; Gupta, T.; Pandya, A. D. Heating effect on C60 films during microfabrication: structure and electrical properties. *Carbon* **2004**, *42* (5−6), 1143−1146.

(52) Kolyadina, E. Y.; Matveeva, L.; Neluba, P.; Shlapatskaya, V. Physical properties of C60 fullerene nanostructures. *Materialwiss. Werkstofftech.* **2013**, *44* (2−3), 144−149.

(53) Lu, K.; Erb, D.; Liu, M. Thermal stability and electrical conductivity of carbon-enriched silicon oxycarbide. *J. Mater. Chem. C* **2016**, *4* (9), 1829−1837.

(54) Kim, K. J.; Eom, J.-H.; Koh, T. Y.; Kim, Y.-W.; Seo, W.-S. Effects of carbon addition on the electrical properties of bulk silicon-oxycarbide ceramics. *J. Eur. Ceram. Soc.* **2016**, *36* (11), 2705−2711.

(55) Cordelair, J.; Greil, P. Electrical conductivity measurements as a microprobe for structure transitions in polysiloxane derived Si-O-C ceramics. *J. Eur. Ceram. Soc.* **2000**, *20* (12), 1947−1957.

(56) Wang, K.; Ma, B.; Li, X.; Wang, Y.; An, L. Effect of pyrolysis temperature on the structure and conduction of polymer-derived SiC. *J. Am. Ceram. Soc.* **2014**, *97* (7), 2135−2138.

(57) Cai, C.; Tao, Z.; Zhu, Y.; Tan, Y.; Wang, A.; Zhou, H.; Yang, Y. A nano interlayer spacing and rich defect 1T-MoS2 as cathode for superior performance aqueous zinc-ion batteries. *Nanoscale Adv.* **2021**, *3* (13), 3780−3787.

(58) Chen, Y.; Yue, M.; Liu, C.; Zhang, H.; Yu, Y.; Li, X.; Zhang, H. Long Cycle Life Lithium Metal Batteries Enabled with Upright Lithium Anode. *Adv. Funct. Mater.* **2019**, *29* (15), 1806752.

(59) Dey, S.; Singh, G. Differentiating Cyclability and Kinetics of Na + Ions in Surface-Functionalized and Nanostructured Graphite Using Electrochemical Impedance Spectroscopy. *Batteries* **2023**, *9*, 534.

(60) Yazami, R.; Reynier, Y. F. Mechanism of self-discharge in graphite-lithium anode. *Electrochim. Acta* **2002**, *47* (8), 1217−1223.

(61) Jiang, C.; Hosono, E.; Zhou, H. Nanomaterials for lithium ion batteries. *Nano Today* **2006**, *1* (4), 28−33.

(62) Jain, R.; Lakhnot, A. S.; Bhimani, K.; Sharma, S.; Mahajani, V.; Panchal, R. A.; Kamble, M.; Han, F.; Wang, C.; Koratkar, N. Nanostructuring versus microstructuring in battery electrodes. *Nat. Rev. Mater.* **2022**, *7* (9), 736−746.

(63) Wang, Z.; Xu, S.; Zhu, X.; Wang, H.; Huang, L.; Yuan, J.; Yang, W. Effects of short-term over-discharge cycling on the performance of commercial 21,700 lithium-ion cells and the identification of degradation modes. *J. Energy Storage* **2021**, *35*, 102257.